Journal of Materials Chemistry A

COMMUNICATION

View Article Online
View Journal | View Issue

Crystalline IrO_2-decorated TiO_2 nanofiber scaffolds for robust and sustainable solar water oxidation†

Cite this: *J. Mater. Chem. A*, 2014, **2**, 5610

Received 20th January 2014
Accepted 29th January 2014

DOI: 10.1039/c4ta00339j

www.rsc.org/MaterialsA

Won-Hee Ryu,‡§ Yang Woo Lee,‡ Yoon Sung Nam, Doo-Young Youn, Chan Beum Park* and Il-Doo Kim*

Crystalline IrO_2 nanoparticles immobilized on TiO_2 nanofiber scaffolds as robust and sustainable oxygen evolving catalysts showed a high turnover number (TON: 322) and excellent recyclability (90% O_2 evolving after 10 cycles). The effects of the decoration position, crystallite size, loading amount of IrO_2, and TiO_2 scaffolds were investigated.

Highly efficient and sustainable water oxidation through solar-driven water-splitting is a key step in the realization of artificial photosynthesis toward mimicking photosystem II in natural photosynthesis.[1–7] Many studies have focused on the development of suitable water oxidation catalysts, mostly based on metal oxides (*e.g.*, IrO_2, RuO_2, Co_3O_4, MnO_2, $LaCoO_3$) owing to their structural and chemical stability and their good catalytic activities.[8–19] In solar-driven water-splitting, photo-generated electrons from a photosensitizer are scavenged by an electron acceptor, and extra holes contained in the photosensitizer are subsequently transferred to a water oxidation catalyst.[20–22] Four cycles of charge transfer between the photosensitizer and the catalyst can oxidize two water molecules while evolving one oxygen molecule.[23] The inherently low reaction rate in water-splitting, which originates from the multiple charge transfer and subsequent O_2 evolving reaction, poses a major barrier that prevents the further improvement of the water oxidation efficiency. Therefore, a tailored design of metal oxide catalysts that enables (1) the rapid extraction of holes from the photosensitizer, (2) the facile transfer of holes to oxygen evolving sites, and (3) the recyclable long-term stability of the catalysts can lead to a breakthrough in artificial photosynthesis.[24,25]

Among various metal oxide-based catalysts, colloidal IrO_2 nanoparticles (NPs) have been considered as promising water oxidation catalysts due to their outstanding catalytic activity.[22,26–29] Colloidal IrO_2 NPs can be easily synthesized through simple hydrolysis of an $IrCl_6^{2-}$ solution.[28,30] However, colloidal IrO_2 NPs in a hydrous form often undergo corrosive surface degradation during multiple water oxidation reactions, degrading the maintenance of their catalytic activity over the long term.[20,31] Furthermore, the charge transfer rate in hydrous IrO_2 catalysts is relatively slow due to the low level of electrical conductivity compared to crystalline IrO_2.[31] Therefore, the crystallization of hydrous IrO_2 catalysts can be an effective means of enhancing their structural resistance and electronic conductivity.

In addition, the catalytic activity of the hydrous IrO_2 catalyst is deteriorated by altering the oxidation states of the Ir element due to the multiple charge transfer which takes place for the oxidation reaction. In the oxygen evolution center of photosystem II in natural photosynthesis, the oxidation states of Mn localized on a Mn–Ca cluster as a catalytic agent can be effectively stabilized by surrounding peptides which supply and regulate the charge carriers during the S state transition, thereby maintaining the catalytic stability of the Mn–Ca cluster.[32] Similarly, for the current water oxidation system, the introduction of a functional scaffold coupling with IrO_2 as a catalyst can prevent the degeneration of the IrO_2 catalysts while also enabling the reuse of the catalysts after several cycles.[33] Furthermore, because tiny IrO_2 NPs tend to aggregate with photosensitizers {*e.g.*, $[Ru(bpy)_3]^{2+}$} upon photo-irradiation to reach the sub-micron scale (~500 nm) clusters,[30] the scaffolds can help to immobilize the IrO_2 NPs uniformly on them. Therefore, finding a suitable scaffold material and structure functionalized by discrete IrO_2 NPs without aggregation is essential for enhancing the catalytic activity.

Here, we introduce a new water oxidation catalytic system for improved oxygen evolution and long-term recyclability by

Department of Materials Science and Engineering, Korea Advanced Institute of Science and Technology, Daejeon 305-701, Republic of Korea. E-mail: idkim@kaist.ac.kr; park3340@kaist.ac.kr; Fax: +82-42-350-3310; Tel: +82-42-350-3326

† Electronic supplementary information (ESI) available: Detailed TEM images, schematic illustrations, XRD analysis, dye-decay experiment and cyclic voltammetry results. See DOI: 10.1039/c4ta00339j

‡ These authors contributed equally to this work.

§ Present address: Department of Chemical and Environmental Engineering, Yale University, New Haven, Connecticut 06520-8286, USA.

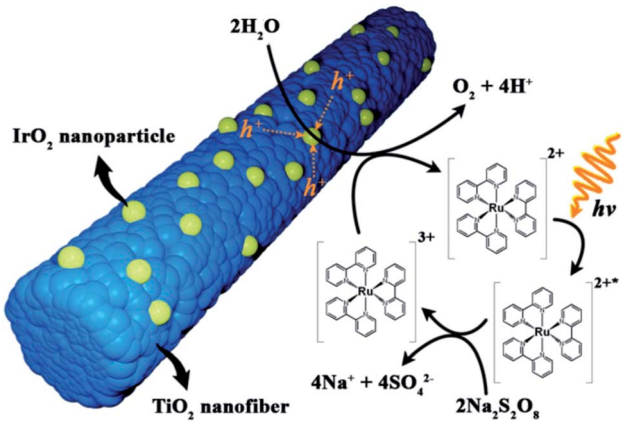

Scheme 1 Schematic illustrations of the photocatalytic water oxidation process by $[Ru(bpy)_3]^{2+}$, $Na_2S_2O_8$ and IrO_2 NP-decorated TiO_2 NFs. Excited electrons in $[Ru(bpy)_3]^{2+*}$ are scavenged by $Na_2S_2O_8$, and the remaining holes are scavenged by IrO_2 NPs on TiO_2 NFs, generating oxygen gas. The TiO_2 NFs act as sacrificial hole donors to the attached IrO_2 NPs, thus facilitating the maintenance of a high oxidation state of the IrO_2 NPs.

combining highly crystalline IrO_2 NPs and TiO_2 nanofiber (NF) scaffolds. As illustrated in Scheme 1, we functionalized crystalline IrO_2 NPs on 1-D TiO_2 NFs synthesized by electrospinning, which is a facile and versatile process for producing webs of long and continuous metal oxide NFs.[34–37] Metallic Ir NPs or hydrous IrO_2 NPs decorated onto TiO_2 NFs were converted to the crystalline IrO_2 phase during an annealing step at 450 °C. We investigated the effects of the decoration position, crystallite size, and loading amount of IrO_2 and verified the long-term cycling capability of the IrO_2-loaded TiO_2 NFs. The role of TiO_2 NFs in solar oxygen evolution was investigated by comparing IrO_2-loaded, semiconducting TiO_2 NFs with IrO_2-loaded, insulating SiO_2 NFs. Our strategy hints at the design of robust and sustainable water oxidation catalysts through the immobilization of metal oxide catalysts on semiconducting 1-D metal-oxide fiber scaffold platforms.

We compared the oxygen-evolving characteristics of pristine TiO_2 NFs, IrO_2–TiO_2 composite NFs (IrO_2–TiO_2 ComNFs) and IrO_2 NP-decorated TiO_2 NFs (IrO_2/TiO_2 NFs). Pristine TiO_2 NFs were synthesized by an electrospinning process followed by calcination at 500 °C. IrO_2–TiO_2 ComNFs were obtained by the electrospinning of an Ir and Ti composite precursor/polyvinylpyrrolidone

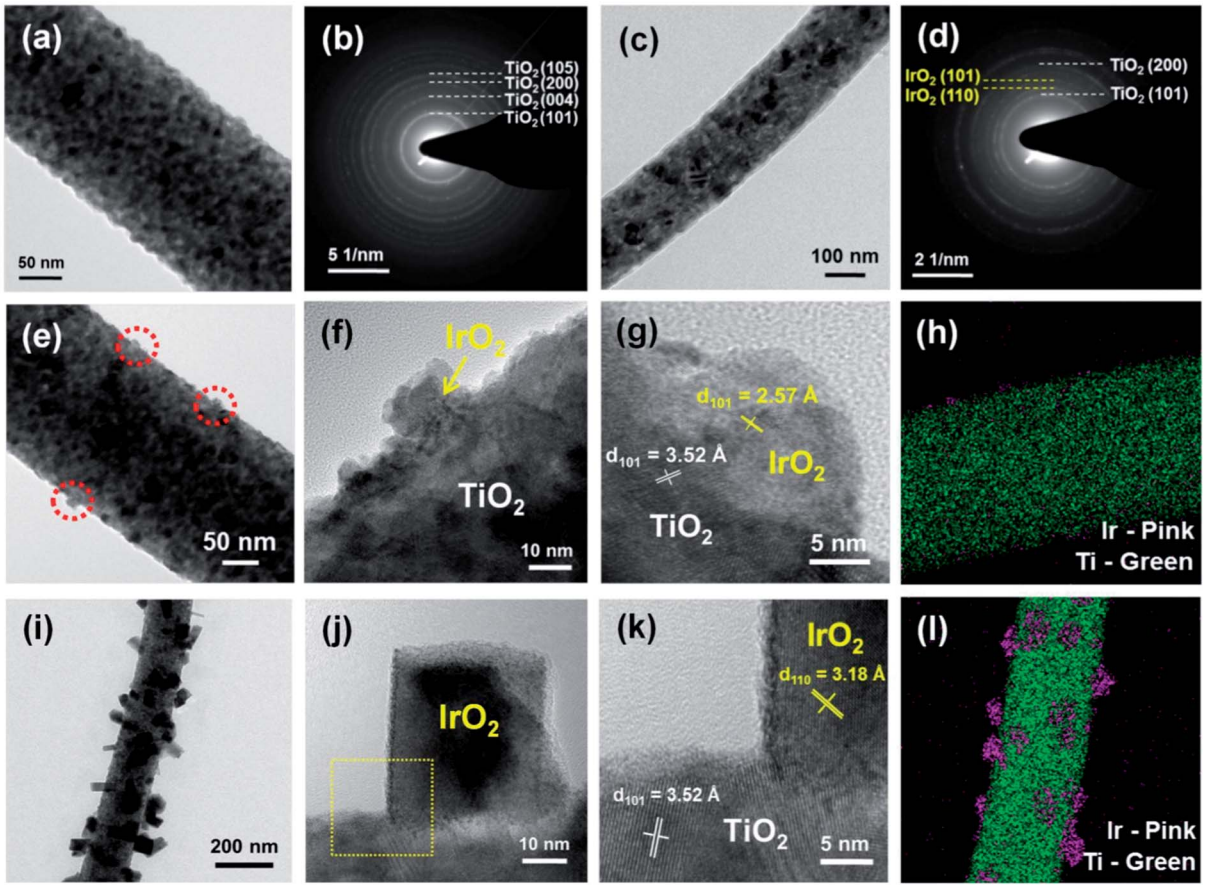

Fig. 1 (a) TEM image and (b) SAED patterns of the TiO_2 NF; (c) TEM images and (d) SAED patterns of the IrO_2–TiO_2 composite NF; (e and f) TEM images and (g) lattice fringe of the IrO_2 NPs (~10 nm) decorated onto the TiO_2 NF with different magnifications; (h) element map of the IrO_2 NPs (~10 nm) decorated onto the TiO_2 NF (iridium – pink, titanium – green); (i and j) TEM images and (k) lattice fringe of the IrO_2 NPs (~30 nm) decorated onto the TiO_2 NF with different magnifications; (l) element map of the IrO_2 NPs (~30 nm) decorated onto the TiO_2 NF (iridium – pink, titanium – green).

(PVP) solution followed by calcination at 500 °C. For the synthesis of the IrO_2 NP-decorated TiO_2 NFs, crystalline IrO_2 NPs were decorated onto the polycrystalline TiO_2 NFs by the attachment of metallic Ir NPs or hydrous IrO_2 NPs on the as-prepared TiO_2 NFs followed by calcination at 450 °C. Fig. 1 shows the micro-structural evolution of the TiO_2 NFs, IrO_2–TiO_2 ComNFs, and IrO_2 NP-decorated TiO_2 NFs. The as-prepared TiO_2 NFs exhibited long and uniform 1-D nanostructures (diameter: 200–300 nm) (Fig. 1a). The indexing of the diffraction ring patterns indicated that they have a polycrystalline TiO_2 structure corresponding to tetragonal I41/amd anatase (Fig. 1b). The IrO_2–TiO_2 ComNFs exhibited a similar 1-D microstructure with a diameter ranging from 150 nm to 200 nm (Fig. 1c), and the diffraction ring patterns suggested a crystalline IrO_2–TiO_2 composite structure (Fig. 1d). The atomic distribution of the Ti and Ir elements was uniform in the nanofibers without any segregation or abnormal particle growth (Fig. S1†). Fig. 1e–h show the microstructure of 10 nm IrO_2 NPs decorated onto TiO_2 NFs; hereafter, we designate these nanofibers as IrO_2/TiO_2 NF-10. The IrO_2 NPs were decorated onto the TiO_2 NFs through the attachment of Ir NPs (crystallite size ~3 nm) with subsequent particle growth in a post-annealing step. The distinct interplanar distances of IrO_2 (2.57 Å) on the outer surface and TiO_2 (3.52 Å) in the nanofiber scaffold corresponded to those of the typical IrO_2 (101) plane (JCPDS no. 86-0330) and TiO_2 (101) plane (JCPDS no. 21-1272), respectively. We confirmed the atomic distribution of the IrO_2 phase (Ir in pink) on the TiO_2 NF (Ti in green) using energy dispersive spectroscopic (EDS) mapping. To investigate the particle size effect of IrO_2, we prepared TiO_2 NFs decorated with 30 nm IrO_2 (*i.e.*, IrO_2/TiO_2 NF-30). IrO_2/TiO_2 NF-30 was prepared using the IrO_2 NPs/PVP complex, which was obtained *via* the purification of a hydrous IrO_2 colloidal solution (Fig. S2†). According to a SEM analysis of IrO_2/TiO_2 NF-30, irregularly shaped IrO_2 NPs of 30 nm size were spatially attached onto the TiO_2 NF backbone (Fig. 1f and g). From the magnified TEM image (the yellow box in Fig. 1j), the interplanar distance of the squared particles was estimated to be approximately 3.18 Å, which is in good agreement with the (110) plane of the IrO_2 phase, while that of the scaffold fibers was about 3.52 Å, corresponding to the (101) plane of the TiO_2 phase (Fig. 1k). We further verified the crystalline structures of pristine TiO_2 NFs, IrO_2–TiO_2 ComNFs, and IrO_2 NP-decorated TiO_2 NFs by means of a XRD analysis, which indicated that the IrO_2/TiO_2 samples were properly formed without any impurity phase (Fig. S5†). In addition, control of the loading amount of IrO_2 NPs on the TiO_2 NFs was utilized to investigate the effect of the amount of IrO_2 NP catalyst. Fig. S3† shows the structural evolution of IrO_2 NP-decorated TiO_2 NFs with varying amounts of IrO_2 (*i.e.*, low amount: IrO_2/TiO_2 NF-10L, high amount: IrO_2/TiO_2 NF-10H).

The changes in the size and distribution of the IrO_2 NPs and TiO_2 NFs significantly affected the photocatalytic water oxidation activity. We compared the water oxidation capacity of pristine TiO_2 NFs, IrO_2–TiO_2 ComNFs, and IrO_2 NP-decorated TiO_2 NFs by varying the IrO_2 particle size and amount with $Na_2S_2O_8$ and $Ru(bpy)_3^{2+}$ (bpy = 2,2′-bipyridine) as an electron acceptor and a photosensitizer, respectively, at pH 8.0 under visible light illumination (λ > 420 nm). The photo-induced $Ru(bpy)_3^{2+}$* generated $Ru(bpy)_3^{3+}$, providing extra holes for water oxidation catalysts, which originated from the larger standard electrode potential of $Ru(bpy)_3^{3+}$/$Ru(bpy)_3^{2+}$ (1.11 V *vs.* NHE at pH 8.0) compared to that of O_2/H_2O (0.76 V *vs.* NHE at pH 8.0). Fig. 2 shows oxygen evolution time profiles during photochemical water oxidation in the presence of each catalyst. The pristine TiO_2 NFs were inactive for water oxidation because the TiO_2 phase has a wide band-gap of ~3.2 eV, which is not suitable for hole injection from $Ru(bpy)_3^{3+}$ and hole transfer to the O_2 evolving site. For the IrO_2–TiO_2 ComNFs, a much lower amount of evolved O_2 was detected when compared with the IrO_2 NP-decorated TiO_2 NF. In oxygen evolution profile, a plateau achieved within 10 min is originated from the deactivation of $[Ru(bpy)_3]^{2+}$ during the photochemical reaction.[38] Although the IrO_2 phase uniformly existed within the composite NFs, the portion of the IrO_2 component exposed to $Ru(bpy)_3^{3+}$ was limited with most of the IrO_2 buried as an inactive phase in the TiO_2 NF structure. Hence, the IrO_2 NP-decorated TiO_2 NF structure, in which IrO_2 NPs were fully exposed on the outer surface of the NFs, was considered as a more suitable structure for photochemical water oxidation.

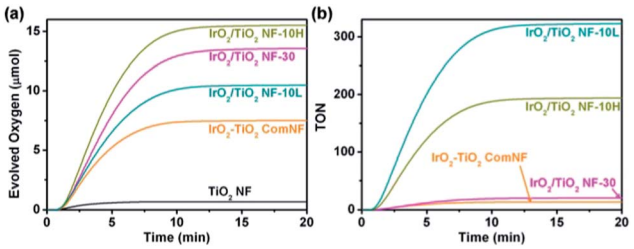

Fig. 2 (a) Time course of the oxygen evolution profile during the photocatalytic water oxidation process with and without IrO_2/TiO_2 NFs using $[Ru(bpy)_2]^{3+}$ and $Na_2S_2O_8$ under visible light illumination (>420 nm). (b) Time course of the turnover number profile. TON was calculated by dividing the amount of evolved oxygen by the amount of iridium oxide in the IrO_2/TiO_2 NFs.

In addition, the effects of the IrO_2 amount and particle size on the catalytic performance of IrO_2 NP-decorated TiO_2 NFs were investigated. The amount of evolved oxygen catalyzed by IrO_2/TiO_2 NF-10 increased with an increase in the loading amount of IrO_2 on the NF scaffold. The NFs with 0.26 wt% of IrO_2 (IrO_2/TiO_2 NF-10L) and 0.72 wt% of IrO_2 (IrO_2/TiO_2 NF-10H) produced 10.49 μmol and 15.56 μmol of oxygen, respectively (Table 1). However, IrO_2/TiO_2 NF-30 produced only 13.56 μmol oxygen despite the much higher loading amount (5.17 wt%) of IrO_2 on the scaffold, which was at least seven times the amount compared to IrO_2/TiO_2 NF-10H. According to a Brunauer–Emmett–Teller (BET) analysis of each sample, the IrO_2/TiO_2 NF-30 sample had a lower surface area, at 18 $m^2\ g^{-1}$, compared to the IrO_2/TiO_2 NF-10 sample, which had a surface area of 31 $m^2\ g^{-1}$ approximately. This indicates that IrO_2/TiO_2 NF-10 provides more active sites for oxygen evolution at the interface than IrO_2/TiO_2 NF-30 due primarily to the smaller particle size. On the other hand, the increased amount of IrO_2 (10 nm) can significantly enhance the hole injection rate from the photosensitizer and lower the overpotential, as confirmed by absorbance decay (Fig. S6†) and electrochemical cyclic

Table 1 Name of the sample, abbreviation, and BET surface area, Ir contents in the NF, the amount of evolved oxygen generated by photocatalytic water oxidation and the calculated turnover number (TON) of each sample; *TON = 4 × $[O_2]$/[catalyst]

Sample name	Abbreviation	BET surface area (m^2 g^{-1})	Ir contents (wt%)	Oxygen evolved (μmol)	TON
TiO_2 nanofiber	TiO_2 NF	31.080	0	5.76	—
IrO_2–TiO_2 composite nanofiber	IrO_2–TiO_2 ComNF	31.076	4.31	7.82	14
IrO_2 nanoparticle (30 nm) decorated TiO_2 nanofiber	IrO_2/TiO_2 NF-30	18.595	5.17	13.56	20
Low amount of IrO_2 nanoparticle (10 nm) decorated TiO_2 nanofiber	IrO_2/TiO_2 NF-10L	31.048	0.26	10.49	322
High amount of IrO_2 nanoparticle (10 nm) decorated TiO_2 nanofiber	IrO_2/TiO_2 NF-10H	31.233	0.62	15.56	195

voltammetric analyses (Fig. S7†). The absorbance decay rate of $Ru(bpy)_3^{3+}$ was much faster in the IrO_2/TiO_2 NF-30 sample as opposed to that of IrO_2/TiO_2 NF-10. The faster reduction of $Ru(bpy)_3^{3+}$ to $Ru(bpy)_3^{2+}$ implies that IrO_2 can rapidly collect photogenerated holes from $Ru(bpy)_3^{3+}$ before the degradation of $Ru(bpy)_3^{3+}$. Furthermore, the cathodic current of IrO_2/TiO_2 NF-30 started at a lower potential (at approximately 1.19 V *vs.* Ag/AgCl) than that of IrO_2/TiO_2 NF-10 (1.3 V), indicating facile hole transfer in the IrO_2 phase to O_2 evolving sites. These results demonstrate that the area of the exposed reaction sites and the amount of the IrO_2 catalyst are the crucial factors for O_2 evolution and hole transfer during photocatalytic water oxidation. For a quantitative evaluation of the catalytic properties of each sample, we calculated the turnover number (TON) based on the iridium content obtained from an inductively coupled plasma-auger electron spectroscopy (ICP-AES) analysis according to the following equation:

$$\text{TON} = \text{amount of evolved } O_2 \times 4/\text{amount of } IrO_2 \text{ catalysts}$$

Note that four times the amount of O_2 evolved per iridium atom is related to the four-hole (electron)-oxidation reaction. Fig. 2b shows the time profile of TONs estimated from the amount of oxygen per IrO_2 amount. The TON of IrO_2/TiO_2 NF-10L was found to be 322, which is much higher than those of the other samples (IrO_2/TiO_2 NF-30: 20 and IrO_2/TiO_2 NF-10H: 193) (Table 1). This result indicates that the water oxidation efficiency per IrO_2 amount can be maximized by attaching smaller particles and lowering the amount of IrO_2 on the TiO_2 NF scaffold.

The hydrous forms of IrO_2 colloids often have insufficient structural stability and low corrosion resistance related to the lower oxidation states of Ir.[39,40] Therefore, the use of crystalline IrO_2 is very important to improve the stability and recyclability of the catalysts for repeated water oxidation. We examined the recyclability of crystalline IrO_2 NP-decorated TiO_2 NFs for photochemical water oxidation. According to our observation, the catalytic activity of crystalline IrO_2 NP-decorated TiO_2 NFs was stably maintained for 10 cycles (Fig. 3a); after 10 cycles, approximately 90% of O_2 was evolved compared to the first cycle. This result shows that crystalline IrO_2 NPs immobilized on a TiO_2 scaffold can collect multiple holes from the photosensitizer and provide O_2 evolving sites without the corrosive surface degradation that easily occurs with hydrous IrO_2 colloids. To verify the stability of the crystalline IrO_2 NPs after the water oxidation reaction, we investigated the structural changes and oxidation state of the as-prepared and first-cycle IrO_2 NPs on TiO_2 NFs using an X-ray photoelectron spectroscopy (XPS) analysis. Typical IrO_2 peaks were observed at 313.1 eV for $4d_{3/2}$ and 297.3 eV for $4d_{5/2}$, in both the as-prepared and first-cycle IrO_2/TiO_2 NF-10L without any peak shift or the appearance of an additional peak (Fig. 3b). This result indicates that the crystalline phase and oxidation state of IrO_2 were stably maintained after the water oxidation reaction. Fig. 3c shows the Ir 4f XPS spectra of the samples. Typical IrO_2 peaks correspond to 64.6 eV for $4f_{5/2}$ and 61.9 eV for $4f_{7/2}$. Although, in the TiO_2 case, a broad peak for Ti 3p overlapped with the peak for Ir $4f_{7/2}$ was observed at near 62 eV,[41,42] a significant difference of XPS peaks was not observed between the as-prepared and the first-cycle

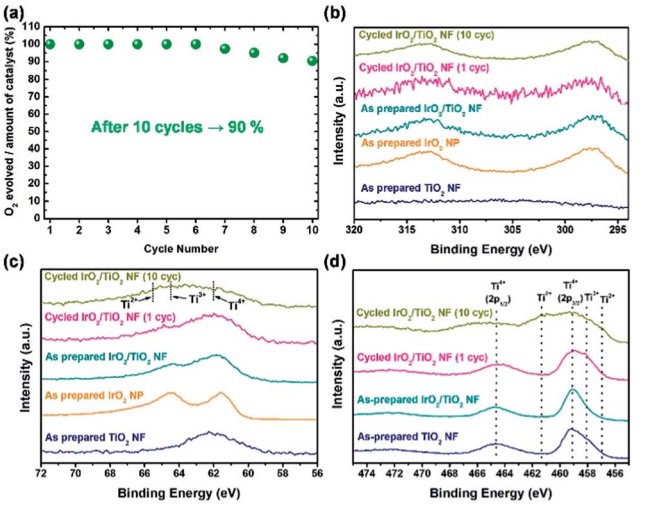

Fig. 3 (a) Cycling test of the evolved oxygen during repeated O_2 evolution testing of IrO_2/TiO_2 NFs. The amount of oxygen which evolved during the repeated experiments was divided by the amount of the catalyst due to the unavoidable partial loss of the catalyst after the O_2 evolving test and subsequent filtration for the next recycling test; (b) Ir 4d (c) Ir 4f and (d) Ti 2p XPS spectra of cycled IrO_2/TiO_2 NFs, as-prepared IrO_2/TiO_2 NFs, as-prepared IrO_2 NPs and as-prepared TiO_2 NFs.

IrO_2/TiO_2 NF-10L samples. However, peak broadening to a higher binding energy of 68 eV was observed after the tenth cycle. When Ti^{4+} is reduced to a low oxidation state, a peak shift to higher binding energy is known to occur. Therefore, peak broadening to a higher binding energy is highly relevant to the partial reduction of Ti during water oxidation, indicating an additional charge supplemented to the IrO_2 NPs. To confirm the interesting phenomenon related to the partial reduction of Ti, the oxidation state of the TiO_2 NF scaffold was investigated from the Ti 2p XPS spectra of the samples (Fig. 3d). Two typical peaks of the Ti 2p XPS spectra corresponding to TiO_2 in the as-prepared IrO_2/TiO_2 NF-10L were observed at 464.7 eV for $2p_{1/2}$ and 459.1 eV for $2p_{3/2}$. However, an additional peak for the first-cycle IrO_2/TiO_2 NF-10L was found at 458.2 eV, which is related to the partial existence of Ti^{3+} in the TiO_2 structure according to the literature.[43] Furthermore, the peaks of Ti^{2+} positioned at 464.7 eV and 457.0 eV as well as the peak of Ti^{3+} were also strengthened after ten cycles. This result demonstrates that the partial reduction of Ti^{4+} in the TiO_2 NF scaffold continuously occurred during repeated O_2 evolving reactions and that the holes in the TiO_2 NFs were subsequently transferred to IrO_2 NP catalysts. The holes supplied from the TiO_2 NFs would not only stabilize the crystalline structure and the oxidation state of IrO_2 but also facilitate the water oxidation reaction by IrO_2 NPs. These unique features mean that the self-reduction of the TiO_2 NF scaffold can maintain the oxidation state of Ir for attached IrO_2 NP catalysts, resulting in enhanced catalytic activity and structural stability.

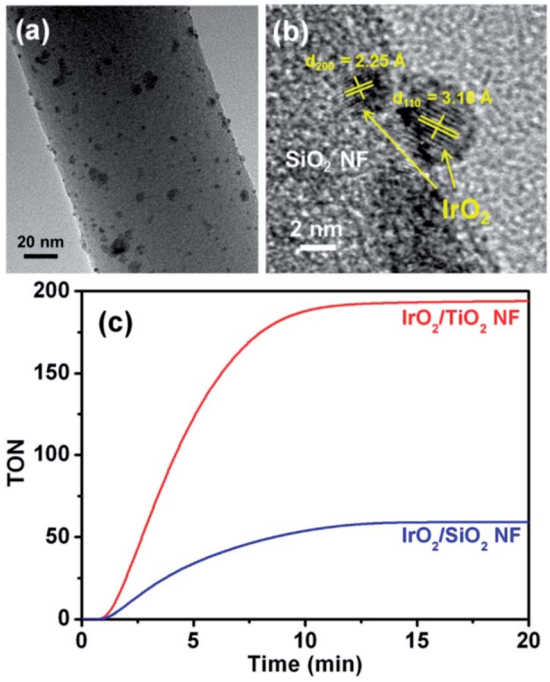

Fig. 4 (a) TEM image and (b) lattice fringe of IrO_2/SiO_2 NFs and (c) time course of the turnover number profile derived from the amount of IrO_2 for IrO_2 NPs (~10 nm) decorated onto the TiO_2 NF and SiO_2 NF scaffolds.

To support our hypothesis that hole supplementation from the TiO_2 scaffold can enhance the water oxidation capability of IrO_2 NPs, we prepared IrO_2 NP-decorated SiO_2 NFs for comparison because SiO_2, which is known to be an insulating material with a wide band gap of ~9.0 eV, exhibits a negligible reduction of Si^{4+} ions. We uniformly decorated IrO_2 NPs (particle size: 2–10 nm) onto SiO_2 NFs (diameter: 150 nm) (Fig. 4a and b). Here, SiO_2 NFs were also synthesized by the electrospinning of Si precursor (TEOS)/PVP composite fibers followed by calcination at 700 °C in air. The crystalline IrO_2 phases existed on the outer surface region of the amorphous SiO_2 NF structure according to the distinct interplanar distances of IrO_2 (2.25 Å and 3.18 Å) corresponding to that of the (200) plane and the (110) plane of the IrO_2 phase (JCPDS no. 86-0330), respectively (Fig. 4b). In a comparison of the O_2-evolving properties of IrO_2/SiO_2 NFs and IrO_2/TiO_2 NFs, the TON (60) of the IrO_2/SiO_2 NFs was much lower than that (195 for IrO_2/TiO_2 NF-10H) of the IrO_2/TiO_2 NFs (Fig. 4c). Furthermore, unlike IrO_2/TiO_2 NFs affording stable recycling properties during 10 cycles, the catalytic activity of IrO_2/SiO_2 NFs became worsened during repeated cycling (Fig. S8†). In the case of IrO_2/SiO_2 NFs, approximately 40% of O_2 was evolved compared with the first cycle after 4 cycles. The result indicates that SiO_2 NFs cannot provide additional holes by self-reduction and thus hole transport pathways for efficient O_2 evolution. Therefore, TiO_2 NFs are more suitable scaffolds for improving the water oxidation capacity of IrO_2 catalysts.

Conclusions

In summary, we succeeded in the synthesis of crystalline IrO_2 NPs decorated onto TiO_2 NF scaffolds for an efficient and recyclable water oxidation catalyst. We investigated the effect of several key factors (*e.g.*, IrO_2 particle size/amount, scaffold fiber type) on photochemical water oxidation. Excellent water oxidation properties were achieved by the controlled immobilization of IrO_2 catalysts on TiO_2 scaffold fibers: (i) IrO_2 sufficiently exposed onto the surface of TiO_2 NFs, (ii) a smaller size of IrO_2 NPs on the TiO_2 NFs, (iii) the use of a low amount of IrO_2 on the TiO_2 NFs, and (iv) suitable selection of the scaffold material (*i.e.*, semi-conducting TiO_2 instead of insulating scaffold fiber). Furthermore, we demonstrated its use as a robust and sustainable catalyst with excellent recyclability (90% O_2 evolving capability after 10 cycles) for repeated water oxidation. Our processing strategy for improving the performance of water oxidation catalysts can be extended to other highly efficient and robust catalyst material systems.

Acknowledgements

This work was supported by a grant from the Center for Inorganic Photovoltaic Materials (2012-0001175) funded by the Korean government (MEST) and by the KAIST Institute for the NanoCentury. This work is supported by the Center for Integrated Smart Sensors funded by the Ministry of Education, Science and Technology as Global Frontier Project (CISS-2012M3A6A6054188).

Notes and references

1 A. W. Rutherford and A. Boussac, *Science*, 2004, **303**, 1782.
2 J. D. Megiatto, Jr, A. Antoniuk-Pablant, B. D. Sherman, G. Kodis, M. Gervaldo, T. A. Moore, A. L. Moore and D. Gust, *Proc. Natl. Acad. Sci. U. S. A.*, 2012, **109**, 15578.
3 H. Inoue, T. Shimada, Y. Kou, Y. Nabetani, D. Masui, S. Takagi and H. Tachibana, *ChemSusChem*, 2011, **4**, 173.
4 J. H. Kim, M. Lee, J. S. Lee and C. B. Park, *Angew. Chem., Int. Ed.*, 2012, **51**, 517.
5 H. Zhou, X. Li, T. Fan, F. E. Osterloh, J. Ding, E. M. Sabio, D. Zhang and Q. Guo, *Adv. Mater.*, 2010, **22**, 951.
6 A. J. Bard and M. A. Fox, *Acc. Chem. Res.*, 1995, **28**, 141.
7 D. K. Bora, A. Braun and E. C. Constable, *Energy Environ. Sci.*, 2013, **6**, 407.
8 Y. Yamada, K. Yano, D. Hong and S. Fukuzumi, *Phys. Chem. Chem. Phys.*, 2012, **14**, 5753.
9 Y. H. Fang and Z. P. Liu, *J. Am. Chem. Soc.*, 2010, **132**, 18214.
10 R. Brimblecombe, A. Koo, G. C. Dismukes, G. F. Swiegers and L. Spiccia, *J. Am. Chem. Soc.*, 2010, **132**, 2892.
11 Q. Mi, R. H. Coridan, B. S. Brunschwig, H. B. Gray and N. S. Lewis, *Energy Environ. Sci.*, 2013, **6**, 2646.
12 Y. Lee, J. Suntivich, K. J. May, E. E. Perry and Y. Shao-Horn, *J. Phys. Chem. Lett.*, 2012, **3**, 399.
13 K. Kalyanasundaram, E. Borgarello and M. Gráutzel, *Helv. Chim. Acta*, 1981, **64**, 362.
14 F. Jiao and H. Frei, *Energy Environ. Sci.*, 2010, **3**, 1018.
15 F. Jiao and H. Frei, *Angew. Chem., Int. Ed. Engl.*, 2009, **48**, 1841.
16 A. G. Scheuermann, J. D. Prange, M. Gunji, C. E. D. Chidsey and P. C. McIntyre, *Energy Environ. Sci.*, 2013, **6**, 2487.
17 X. L. Huang, J. Chai, T. Jiang, Y. J. Wei, G. Chen, W. Q. Liu, D. X. Han, L. Niu, L. M. Wang and X. B. Zhang, *J. Mater. Chem.*, 2012, **22**, 3404.
18 S. C. Riha, B. M. Klahr, E. C. Tyo, S. Seifert, S. Vajda, M. J. Pellin, T. W. Hamann and A. B. F. Martinson, *ACS Nano*, 2013, **7**, 2396.
19 J. Zhu, Z. Yin, D. Yang, T. Sun, H. Yu, H. E. Hoster, H. H. Hng, H. Zhang and Q. Yan, *Energy Environ. Sci.*, 2013, **6**, 987.
20 Y. S. Nam, A. P. Magyar, D. Lee, J. W. Kim, D. S. Yun, H. Park, T. S. Pollom, Jr, D. A. Weitz and A. M. Belcher, *Nat. Nanotechnol.*, 2010, **5**, 340.
21 Z. Huang, Z. Luo, Y. V. Geletii, J. W. Vickers, Q. Yin, D. Wu, Y. Hou, Y. Ding, J. Song, D. G. Musaev, C. L. Hill and T. Lian, *J. Am. Chem. Soc.*, 2011, **133**, 2068.
22 M. Hara, C. C. Waraksa, J. T. Lean, B. A. Lewis and T. E. Mallouk, *J. Phys. Chem. A*, 2000, **104**, 5275.
23 T. A. Betley, Q. Wu, T. Van Voorhis and D. G. Nocera, *Inorg. Chem.*, 2008, **47**, 1849.
24 S. D. Tilley, M. Cornuz, K. Sivula and M. Grätzel, *Angew. Chem., Int. Ed.*, 2010, **122**, 6549.
25 W. J. Youngblood, S.-H. A. Lee, K. Maeda and T. E. Mallouk, *Acc. Chem. Res.*, 2009, **42**, 1966.
26 Y. X. Zhao, E. A. Hernandez-Pagan, N. M. Vargas-Barbosa, J. L. Dysart and T. E. Mallouk, *J. Phys. Chem. Lett.*, 2011, **2**, 402.
27 T. Kuwabara, E. Tomita, S. Sakita, D. Hasegawa, K. Sone and M. Yagi, *J. Phys. Chem. C*, 2008, **112**, 3774.
28 P. G. Hoertz, Y. I. Kim, W. J. Youngblood and T. E. Mallouk, *J. Phys. Chem. B*, 2007, **111**, 6845.
29 L. Badia-Bou, E. Mas-Marza, P. Rodenas, E. M. Barea, F. Fabregat-Santiago, S. Gimenez, E. Peris and J. Bisquert, *J. Phys. Chem. C*, 2013, **117**, 3826.
30 M. Hara, J. T. Lean and T. E. Mallouk, *Chem. Mater.*, 2001, **13**, 4668.
31 L. D. Burke and D. P. Whelan, *J. Electroanal. Chem.*, 1984, **162**, 121.
32 R. J. Debus, *Coord. Chem. Rev.*, 2008, **252**, 244.
33 L. Mai, F. Dong, X. Xu, Y. Luo, Q. An, Y. Zhao, J. Pan and J. Yang, *Nano Lett.*, 2013, **13**, 740.
34 D. Li, Y. L. Wang and Y. N. Xia, *Nano Lett.*, 2003, **3**, 1167.
35 I. D. Kim, A. Rothschild, B. H. Lee, D. Y. Kim, S. M. Jo and H. L. Tuller, *Nano Lett.*, 2006, **6**, 2009.
36 V. Thavasi, G. Singh and S. Ramakrishna, *Energy Environ. Sci.*, 2008, **1**, 205.
37 D. J. Yang, I. Kamienchick, D. Y. Youn, A. Rothschild and I. D. Kim, *Adv. Funct. Mater.*, 2010, **20**, 4258.
38 F. Song, Y. Ding, B. Ma, C. Wang, Q. Wang, X. Du, S. Fu and J. Song, *Energy Environ. Sci.*, 2013, **6**, 1170.
39 A. Harriman, I. J. Pickering, J. M. Thomas and P. A. Christensen, *J. Chem. Soc., Faraday Trans. 1*, 1988, **84**, 2795.
40 L. D. Burke and D. P. Whelan, *J. Electroanal. Chem.*, 1981, **124**, 333.
41 M. Oku, K. Wagatsuma and S. Kohiki, *Phys. Chem. Chem. Phys.*, 1999, **1**, 5327.
42 Z. S. Li, J. H. Jorgensen, P. J. Moller, M. Sambi and G. Granozzi, *Appl. Surf. Sci.*, 1999, **142**, 135.
43 S. Hashimoto and A. Tanaka, *Surf. Interface Anal.*, 2002, **34**, 262.